NIH Public Access
Author Manuscript
Phys Med Biol. Author manuscript; available in PMC 2013 August 19.

Published in final edited form as:
Phys Med Biol. 2010 May 7; 55(9): 2669–2677. doi:10.1088/0031-9155/55/9/016.

Quantitative imaging of electron density and effective atomic number using phase contrast CT

Zhihua Qi[1], **Joseph Zambelli**[1], **Nicholas Bevins**[1], and **Guang-Hong Chen**[1,2]

Guang-Hong Chen: gchen7@wisc.edu

[1]Department of Medical Physics, University of Wisconsin-Madison, WI 53705, USA

[2]Department of Radiology, University of Wisconsin-Madison, WI 53792, USA

Abstract

Compared to single energy CT, which only provides information for x-ray linear attenuation coefficients, dual-energy CT is able to obtain both the electron density and effective atomic number for different materials in a quantitative way. In this study, as an alternative to dual-energy CT, a novel quantitative imaging method based on phase contrast CT is presented. Rather than requiring two projection data sets with different x-ray energy spectra, diffraction-grating-based phase contrast CT is capable of reconstructing images of both linear attenuation and refractive index decrement from the same projection data using a single x-ray energy spectra. From the two images, quantitative information of both the electron density and effective atomic number can be extracted. Two physical phantoms were constructed and used to validate the presented method. Experimental results demonstrate that (1) electron density can be accurately determined from refractive index decrement through a linear relationship, and (2) the effective atomic number can be explicitly derived from the ratio of the linear attenuation to refractive index decrement using a power function plus a constant. The presented method will provide insight into the technique of material separation and find its use in medical and industrial applications.

1. Introduction

X-ray computed tomography (CT) is an imaging modality that is able to reconstruct an image of the distribution of linear attenuation coefficients within the scanned object. The linear attenuation coefficient describes how much a material attenuates the intensity of the incident x-ray beam of a certain energy, and its difference over different types of materials provides the contrast needed for the task of material separation in medical diagnosis, luggage inspection and other applications. However, the fact that materials of different chemical compositions may possess quite similar linear attenuation coefficients significantly limits the capability of single energy CT-based material differentiation. This problem is mostly caused by the dependence of linear attenuation coefficient on two more basic physical quantities, electron density, ρ_e, and the effective atomic number, Z_{eff}. The poor soft tissue contrast in CT is partially a result of the fact that various tissues may have similar attenuation properties, despite having different ρ_e or Z_{eff}. This calls for the capability of decomposing the linear attenuation coefficient into ρ_e and Z_{eff}. In addition, quantitative information about ρ_e and Z_{eff} is quite valuable in many applications. For instance, ρ_e plays a key role in treatment planning in image-guided radiation therapy, while Z_{eff} serves as a very important index for explosive detection.

Dual-energy CT, as a solution to reconstruct the distribution of both ρ_e and Z_{eff}, was proposed in the 1970s (Alvarez and Macovski 1976) and has been used in related applications. The image object is scanned with x-ray beams of different energy spectra. With two sets of measurements available, ρ_e and Z_{eff} can be extracted mathematically. The

NIH-PA Author Manuscript
NIH-PA Author Manuscript
NIH-PA Author Manuscript

NIH-PA Author Manuscript

NIH-PA Author Manuscript

NIH-PA Author Manuscript

difference between the two energy spectra dictates the quality of the solutions of ρ_e and Z_{eff}; namely, the more similar the two x-ray spectra, the more the results suffer from noise. Ideally, the two x-ray beams would be monochromatic at two different energies to ensure the best separability, which would be available only at synchrotron facilities (Torikoshi *et al* 2003).

In this paper, an innovative quantitative imaging method using phase contrast CT is presented as an alternative to dual-energy CT for the calculation of ρ_e and Z_{eff}. In recent years, phase contrast x-ray imaging and its CT counterpart (Davis *et al* 1995, Wilkins *et al* 1996, Chapman *et al* 1997, Momose *et al* 1996, Dilmanian *et al* 2000, Pfeiffer *et al* 2006, 2007) have been developed by taking advantage of the wave properties of x-rays. By reconstructing the decrement of the real part of the index of refraction in different materials from projection data, which is directly correlated with electron density (Bech *et al* 2009), phase contrast CT offers a new contrast mechanism for material differentiation. In addition to phase contrast information, the same acquired projection data set can be used to reconstruct attenuation coefficients as well. Thus, the differential phase contrast experimental setup provides multiple imaging contrast mechanisms and enables extraction of mutual information from them. In this paper, we will present how to use the two contrast mechanisms, x-ray attenuation and phase contrast, to simultaneously extract the electron density and effective atomic number for accurate material classifications. As a result, differential phase contrast CT offers a new solution for quantitative measurement of the electron density and effective atomic number. The key difference between the presented method and dual-energy CT is that the former can extract both the electron density and effective number from the same projection data set using a single x-ray spectrum, i.e. there is no need for a separate projection data set with a different energy spectrum.

2. Methods

2.1. Basic physical principles

The behavior of an x-ray when passing through an object is determined by the refractive index of the object. The refractive index is described by $n = 1 - \delta + i\beta$. The decrement of the real part of the refractive index, δ, describes the x-ray phase shift, whereas the imaginary part, β, describes the attenuation and is proportional to the linear attenuation coefficient, μ, by $\mu = 4\pi\lambda^{-1}\beta$. In conventional x-ray CT, only μ (or β equivalently) of the object is measured, while in phase contrast CT, one is able to obtain information for both δ and β. δ is related to the electron density, ρ_e, and energy, E, according to

$$\delta = \frac{\rho_e r_0 \hbar^2 c^2}{2\pi E^2}, \quad (1)$$

where $r_0 = 2.82 \times 10^{-15}$ m is the classical radius of the electron, ħ is the reduced Planck constant and c is the speed of light. It is easily seen that ρ_e can be directly retrieved from δ through a linear relationship.

Once the electron density information is known, the effective atomic number Z_{eff} can be extracted from the attenuation coefficient μ. In the diagnostic x-ray energy range, the x-ray linear attenuation of an object at a certain energy E is composed mainly of two parts: the photoelectric cross section σ_{pe} and the scattering cross section σ_{sc}. A mathematical description of the x-ray linear attenuation coefficient is given by

NIH-PA Author Manuscript

NIH-PA Author Manuscript

NIH-PA Author Manuscript

$$\mu=\rho\frac{N_A}{A}(\sigma_{\mathrm{pe}}+\sigma_{\mathrm{sc}}), \quad (2)$$

where ρ, N_{A} and A are the mass density, Avogadro's number and atomic mass, respectively. σ_{pe} is approximated as

$$\sigma_{\mathrm{pe}}\sim\frac{Z^m}{E^3}, \quad (3)$$

where m is a constant. σ_{sc} is described as a combination of the Compton and coherent scattering cross sections as

$$\sigma_{\mathrm{sc}}=Z[\Phi_{\mathrm{KN}}(E)+\Phi_{\mathrm{coh}}(Z,E)], \quad (4)$$

where $\Phi_{\mathrm{KN}}(E)$ and $\Phi_{\mathrm{coh}}(Z, E)$ are the Klein–Nishina cross section and the coherent scattering cross section, respectively. By making use of the expression of the electron density $\rho_{\mathrm{e}} = \rho N_{\mathrm{A}} Z/A$, equation (2) can be rewritten as

$$\mu=\rho_e\left[K\frac{Z^{m-1}}{E^3}+\Phi_{\mathrm{KN}}(E)+\Phi_{\mathrm{coh}}(Z,E)\right], \quad (5)$$

where K is a constant. If the contribution of coherent scattering to the total x-ray attenuation is negligible, equation (5) is further reduced to

$$\mu=\rho_e\left[K\frac{Z^{m-1}}{E^3}+\Phi_{\mathrm{KN}}(E)\right]. \quad (6)$$

In order to separate Z information from ρ_{e}, an index is proposed as the ratio between μ and δ:

$$\frac{\mu}{\delta}=\left[K\frac{Z^{m-1}}{E^3}+\Phi_{\mathrm{KN}}(E)\right]\frac{2\pi E^2}{r_0\hbar^2c^2}=p\times Z^n+q, \quad (7)$$

where p and q are constants, $n = m - 1$ is a constant, and energy-related terms may be taken as constants because the x-ray energy spectrum is fixed for a given scan. Equation (7) reveals that the μ/δ ratio is related to Z of a certain material (replaced by Z_{eff} for compositions) in an explicit functional form, i.e. a power function plus a constant, and such a relationship can be used to measure Z_{eff} for scanned materials.

2.2. Experimental phantoms and data acquisition system

Two contrast phantoms containing several types of plastic were constructed for quantitative measurement and evaluation. The cross sections of the two contrast phantoms are shown in figure 1. In the first phantom, the PTFE (polytetrafluroethylene), PMMA (poly(methyl methacrylate)) and POM (polyoxymethylene) rods are all 4.76 mm in diameter; the air-filled tube has an inner diameter of 6.60 mm and a wall thickness of 0.80 mm, and the phantom chamber has an inner diameter of 25.4 mm and a wall thickness of 1.55 mm. In the second phantom, the LDPE (low density polyethylene), PS (polystyrene) and PMMA rods are all 6.2 mm in diameter, and the phantom chamber has an inner diameter of 22.2 mm and a wall thickness of 1.65 mm. The chemical formulae of the materials used in the two phantoms are

NIH-PA Author Manuscript

NIH-PA Author Manuscript

NIH-PA Author Manuscript

listed in table 1, and it is from the chemical compositions of these materials that the Z_{eff} values are calculated.

The phantoms were scanned by an experimental phase contrast imaging system constructed at the University of Wisconsin-Madison. The system uses the previously reported grating interferometer method (Weitkamp *et al* 2005) to obtain the phase shift of x-rays as they propagate through a sample of interest.

The system subcomponents used in the experimental setup include x-ray gratings, a rotating-anode x-ray tube, a flat-panel x-ray detector and a rotating motion stage to enable tomographic acquisitions. The x-ray tube used is a Varian G1592 with a 1.2 mm nominal focal spot size, which is connected to a CPI Indico 100 generator. The detector is a Radicon Shad-o-Box 2048, with 48 × 48 μm^2 pixels across a 1024 × 2048 array. The three gratings are fabricated using the techniques described in the literature (David *et al* 2007). The first grating, labeled G_0, is an absorption grating with a pitch of 37 μm and a duty cycle of 40.5%, which divides the x-ray beam exiting from the tube into an array of spatially coherent line sources, allowing the use of large focal spot (≈1 mm) x-ray sources. The second grating, G_1, is a phase grating with a pitch of 8 μm and a duty cycle of 50%, fabricated using a wet-etch procedure in Si. G_1 is designed to introduce a π phase shift at the mean energy of the x-ray beam for half of the incident x-rays. The final grating, G_2, is an absorption grating with a pitch of 4.5 μm and a duty cycle of 50%, fabricated the same way as G_1, but with the additional step of electroplating gold into the grating slits. This grating acts as an analyzer so that the replicated fringe pattern from G_1 is converted to an intensity distribution at the detector plane. The fringe pattern occurs with a spatial period of 4.5 μm, which is too small to be resolved directly. In order to measure intensity modulation at the detector plane, a phase stepping approach is used (Weitkamp *et al* 2005, Pfeiffer *et al* 2006, 2007). In this work, eight phase steps were used, sampled over the 4.5 μm period.

The scan was performed in a CT acquisition mode, in which 360 projections were taken at 1° increments with eight phase steps per projection. Each projection had an exposure time of approximately 80 s. The tube voltage was set to 40 kVp, with a continuous tube current of 10 mA. The source-to-isocenter distance was 1561 mm, and the source-to-detector distance was 1882 mm.

As a result of the cone beam geometry of the imaging system, both the attenuation and phase contrast images are reconstructed by FDK-type reconstruction algorithms (Feldkamp *et al* 1984). However, the reconstruction of the attenuation image is done by directly applying the FDK algorithm commonly used in attenuation CT, whereas the phase contrast image is reconstructed by extending a fan beam reconstruction algorithm for differential phase contrast CT to the 3D case (Qi and Chen 2008). The reconstructed image matrix is 400 × 400 × 400, with a voxel size of (100 μm)^3 for the first phantom, and 500 × 500 × 250, with a voxel size of (80 μm)^3 for the second.

3. Results

3.1. Reconstructed images

Reconstructed images of μ and δ, along with the image of their ratio, for the two phantoms are shown in figures 2 and 3. As introduced in the previous section, the δ and μ/δ images essentially give the distribution of ρ_e and Z_{eff}, respectively. One of the most striking differences across the μ, δ and μ/δ images comes from the PMMA rod. There is little contrast between PMMA and the water in the μ image, due to the fact that their μ values are very close at the beam energy used. However, the PMMA-to-water contrast is larger in both the δ and μ/δ images. More interestingly, the contrast is reversed in these two images. This

NIH-PA Author Manuscript

NIH-PA Author Manuscript

NIH-PA Author Manuscript

observation explains why their μ values are similar: μ is determined by both ρ_e and Z_{eff}. This demonstrates the importance of obtaining both ρ_e and Z_{eff} information. In figure 3, the δ image shows little contrast between the PS rod and the surrounding water. In this case, the ρ_e provides limited contrast to differentiate PS from water; however, the μ and μ/δ images considerably enhance the PS-to-water contrast due to the pronounced difference of Z_{eff} between the two materials. This further demonstrates the need to simultaneously have both ρ_e and Z_{eff} for better material differentiation capabilities.

3.2. Quantitative measurement of ρ_e

A comparison was made between the electron densities derived from the CT images and reference electron densities. The reference ρ_e values were calculated by the equation $\rho_e = \rho N_A Z/A$. The electron densities from the CT images were determined by the following steps.

1. ROIs were selected within each material in the slice image and the mean δ values were measured.
2. The mean x-ray beam energy was calibrated by finding which energy gives a calculated electron density of water using equation (1) which is equal to its reference electron density.
3. The electron densities of the other materials were calculated using the calibrated x-ray beam energy and equation (1).

The electron density values measured from the CT images as well as the corresponding reference values are listed in table 2 and plotted in figure 4(a). The standard deviation of the electron density values within the selected ROI is used as an error estimate. The plot shows a linear relationship for the first five materials, while the slope decreases for PTFE. This decrease could be caused by (1) uncertainty of the exact mass densities for the phantom materials, which are needed for the calculation of reference ρ_e; (2) pronounced beam hardening effects for high-Z materials (PTFE in this case) due to the polychromatic nature of the x-ray beam used.

All data points except PTFE were fitted to a linear function, i.e. $\rho_e^{cal} = a \times \rho_e^{ref} + b$ by a least-squares fit, and the fitted line is shown in figure 4(a). The parameters of the fitted line are $a = 1.0055$ and $b = -0.0123 \times 10^{23}$ cm^{-1}, and the correlation coefficient between the experimental and fitted data points is 0.9998. This demonstrates the quantitative accuracy of phase contrast CT in the measurement of electron density.

3.3. Quantitative relationship between μ/δ and Z_{eff}

The effective atomic number Z_{eff} was calculated by the following equation (Spiers 1946):

$$Z_{eff} = \sqrt[2.94]{\sum_i f_i \times (Z_i)^{2.94}}, \quad (8)$$

where f_i is the fraction of the total number of electrons associated with each element, and Z_i is the atomic number of each element. The values of μ/δ and Z_{eff} are tabulated in table 2 and plotted in figure 4(b). The standard deviation of μ/δ values within the selected ROI is used as an error estimate. In order to determine the quantitative relationship between Z_{eff} and μ/δ, a nonlinear optimization was applied to achieve a least-squares fit of all data points to the function form in equation (7). The fitted curve is shown in figure 4(b). The parameters were $n = 3.906$, $p = 21.19$ cm^{-1} and $q = 7.375 \times 10^5$ cm^{-1}. The correlation coefficient between the experimental and fitted data points was 0.9991. The fitted curve agrees well with the

NIH-PA Author Manuscript

NIH-PA Author Manuscript

NIH-PA Author Manuscript

experimental data points. The agreement between the experimental data points and the fitted curve proves the validity of equation (7); furthermore, it demonstrates that Z_{eff} can be quantitatively measured from phase contrast CT images using a simple function in the form of a power function plus a constant.

4. Discussions

In this study, we hypothesized that the x-ray attenuation caused by coherent scattering could be ignored, because coherent scatter accounts for only about 10% of the total interactions for the mean beam energy (≈28 keV) used in this experiment. Additionally, as a higher x-ray beam energy is used, which is the future direction of this technique to improve photon statistics, the relative contribution from coherent scattering will decrease further. Our hypothesis was validated by the excellent agreement between the proposed model (equation (7)) and the experimental data points, as shown in figure 4(b).

The proposed model demonstrated its accuracy in describing the relationship between μ/δ and Z_{eff} for the group of materials being studied under certain experimental conditions; for other materials under different conditions, the parameters of the model may vary, and the model may need modification to incorporate new physical effects. For example, for high-Z materials which have photoelectric absorption edges within the x-ray energy spectrum, a more complex functional form would be necessary.

5. Conclusion

A novel quantitative imaging method using phase contrast CT is presented. By conducting a scan of a contrast phantom using a differential phase contrast CT setup, the method is validated to be able to provide quantitative information for both ρ_e and Z_{eff}. ρ_e can be calculated from δ through a linear relationship; Z_{eff} is proven to relate to μ/ρ through a simple function, and therefore can be explicitly derived. Although a grating-based differential phase contrast CT setup is employed for experimental validation, the method of obtaining the electron density and effective atomic number is also applicable to the other types of x-ray phase contrast CT systems (e.g., diffraction enhanced imaging, in-line holography and others). For a comprehensive investigation on determination of the effective atomic number, a wider Z range of materials need to be studied, and beam hardening should be carefully dealt with to find a more accurate description of the relationship between μ/δ and Z_{eff}. In conclusion, phase contrast CT shows promise for quantitative imaging of the electron density and effective atomic number, and as a result, offers an alternative to dual-energy CT for applications related to material differentiation.

References

Alvarez RE, Macovski A. Energy-selective reconstructions in x-ray computerised tomography. Phys Med Biol. 1976; 21:733–44. [PubMed: 967922]

Bech M, Jensen TH, Feidenhans'l R, Bunk O, David C, Pfeiffer F. Soft-tissue phase-contrast tomography with an x-ray tube source. Phys Med Biol. 2009; 54:2747–53. [PubMed: 19369710]

Chapman D, Thomlinson W, Johnston RE, Washburn D, Pisano E, Gmur N, Zhong Z, Menk R, Arfelli F, Sayers D. Diffraction enhanced x-ray imaging. Phys Med Biol. 1997; 42:2015–25. [PubMed: 9394394]

David C, Bruder J, Rohbeck T, Grüzweig C, Kottler C, Diaz A, Bunk O, Pfeiffer F. Fabrication of diffraction gratings for hard x-ray phase contrast imaging. Microelec Eng. 2007; 84:1172–7.

Davis TJ, Gao D, Gureyev TE, Stevenson AW, Wilkins SW. Phase-contrast imaging of weakly absorbing materials using hard x-rays. Nature. 1995; 373:595–8.

NIH-PA Author Manuscript

NIH-PA Author Manuscript

NIH-PA Author Manuscript

Dilmanian FA, Zhong Z, Ren B, Wu XY, Chapman LD, Orion I, Thomlinson WC. Computed tomography of x-ray index of refraction using the diffraction enhanced imaging method. Phys Med Biol. 2000; 45:933–46. [PubMed: 10795982]

Feldkamp LA, Davis LC, Kress JW. Practical cone-beam algorithm. J Opt Soc Am A. 1984; 1:612–9.

Momose A, Takeda T, Itai Y, Hirano K. Phase-contrast x-ray computed tomography for observing biological soft tissues. Nat Med. 1996; 2:473–5. [PubMed: 8597962]

Pfeiffer F, Weitkamp T, Bunk O, David C. Phase retrieval and differential phase-contrast imaging with low-brilliance x-ray sources. Nat Phys. 2006; 2:258–61.

Pfeiffer F, Kottler C, Bunk O, David C. Hard x-ray phase tomography with low-brilliance sources. Phys Rev Lett. 2007; 98:108105. [PubMed: 17358572]

Qi Z, Chen G-H. Direct fan-beam reconstruction algorithm via filtered backprojection for differential phase-contrast computed tomography. X-ray Opt Instrum. 2008; 2008:835172.

Spiers FW. Effective atomic number and energy absorption in tissues. Br J Radiol. 1946; 19:52–63. [PubMed: 21015391]

Torikoshi M, Tsunoo T, Sasaki M, Endo M, Noda Y, Ohno Y, Kohno T, Hyodo K, Uesugi K, Yagi N. Electron density measurement with dual-energy x-ray CT using synchrotron radiation. Phys Med Biol. 2003; 48:673–85. [PubMed: 12696802]

Weitkamp T, Diaz A, David C, Pfeiffer F, Stampanoni M, Cloetens P, Zeigler E. X-ray phase imaging with a grating interferometer. Opt Express. 2005; 12:6296–304. [PubMed: 19498642]

Wilkins SW, Gureyev TE, Gao D, Pogany A, Stevenson AW. Phase-contrast imaging using polychromatic hard x-rays. Nature. 1996; 384:335–8.

NIH-PA Author Manuscript

NIH-PA Author Manuscript

NIH-PA Author Manuscript

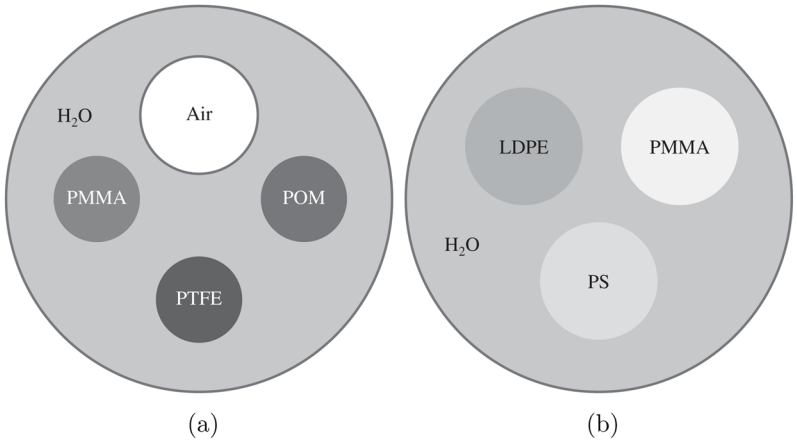

Figure 1.
Illustrations of the two experimental phantoms. In the first phantom (a), three plastic rods and one air-filled plastic tube were placed in a water-filled plastic cylinder. In the second phantom (b), three plastic rods were placed in a water-filled plastic cylinder.

NIH-PA Author Manuscript

NIH-PA Author Manuscript

NIH-PA Author Manuscript

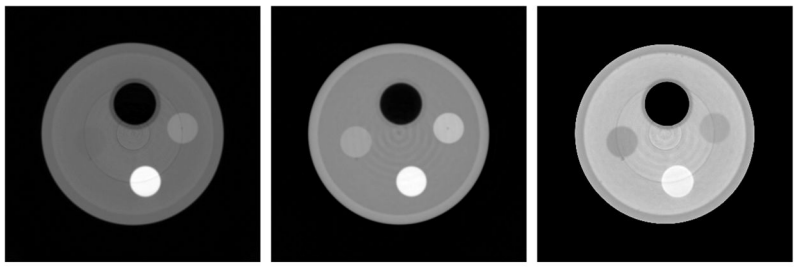

Figure 2.

The images of three different physical quantities obtained from a differential phase contrast CT scan of the first phantom. From left to right are the images of μ (display window: [0 0.85] cm^{-1}), δ (display window [0 0.53] $\times 10^{-6}$) and μ/δ (display window [0 1.70] $\times 10^{5}$ cm^{-1}), respectively. The arrangement of the phantom materials is shown in figure 1(a).

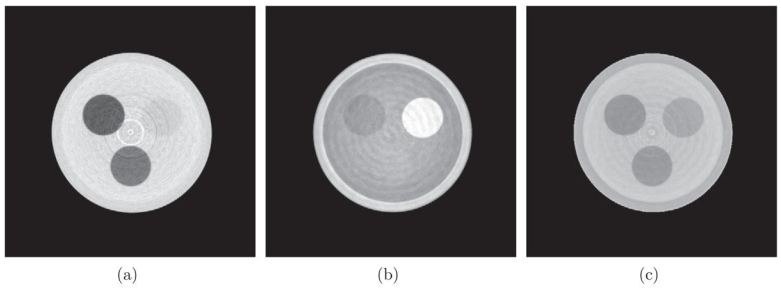

Figure 3.
The images of three different physical quantities obtained from a differential phase contrast CT scan of the second phantom. From left to right are the images of μ (display window [0.20 0.40] cm^{-1}), δ (display window [0.20 0.35] $\times 10^{-6}$) and μ/δ (display window [0 1.70] $\times 10^5$ cm^{-1}), respectively. The arrangement of the phantom materials is shown in figure 1(b).

NIH-PA Author Manuscript
NIH-PA Author Manuscript
NIH-PA Author Manuscript

NIH-PA Author Manuscript

NIH-PA Author Manuscript

NIH-PA Author Manuscript

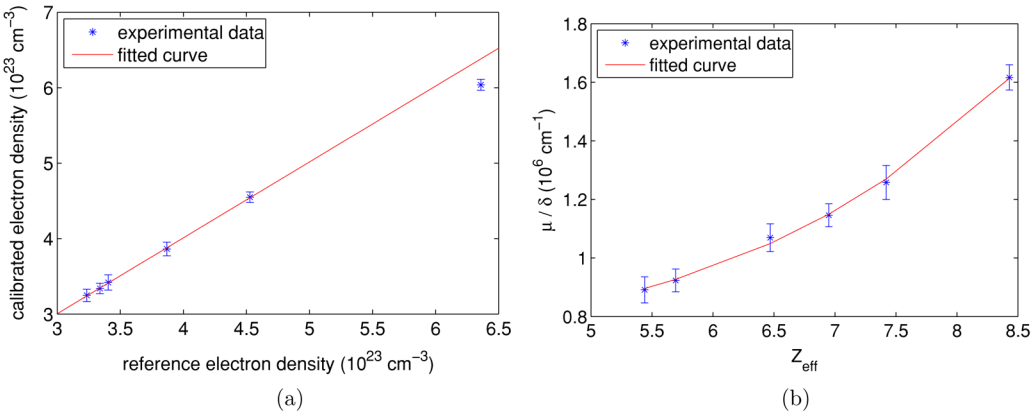

Figure 4.

Plots of quantitative measurements for different materials and fitted curves. In (a) data points from left to right are LDPE, water, PS, PMMA, POM and PTFE, respectively; the fitted curve is a straight line for all data points except PTFE. In (b), data points from left to right are LDPE, PS, PMMA, POM, water and PTFE, respectively; a curve in the form of equation (7) was fitted over all data points. (a) ρ_e^{cal} versus ρ_e^{ref} (b) μ/δ versus Z_{eff}.

NIH-PA Author Manuscript
NIH-PA Author Manuscript
NIH-PA Author Manuscript

Table 1

The chemical formulae of the materials used for quantitative measurements.

	Water	PMMA	POM	PTFE	LDPE	PS
Chemical formula	H_2O	$(C_5O_2H_8)_n$	$(CH_2O)_n$	$(C_2F_4)_n$	$(C_2H_4)_n$	$(C_8H_8)_n$

NIH-PA Author Manuscript NIH-PA Author Manuscript NIH-PA Author Manuscript

Table 2

Quantitative measurement results for the reconstructed images of both attenuation contrast and phase contrast. ρ_e^{ref} and ρ_e^{cal} are reference electron density and calibrated electron density, respectively.

	μ(cm^{-1})	δ (10^{-6})	$\rho_e^{\mathrm{ref}}(10^{23}\mathrm{cm}^{-3})$ (10^{23} cm^{-3})	$\rho_e^{\mathrm{cal}}(10^{23}\mathrm{cm}^{-3})$ (10^{23} cm^{-3})	μ/δ (10^5 cm^{-1})	Z_{eff}
Water	0.361	0.287	3.34	3.34	1.26	7.42
PMMA	0.355	0.332	3.87	3.86	1.07	6.47
POM	0.448	0.391	4.53	4.55	1.15	6.95
PTFE	0.839	0.519	6.36	6.04	1.62	8.43
LDPE	0.254	0.285	3.23	3.25	0.891	5.44
PS	0.277	0.300	3.40	3.42	0.923	5.70

Phys Med Biol. Author manuscript; available in PMC 2013 August 19.